Research Article Vol. 33, No. 11 / 2 Jun 2025 / Optics Express 22208

Optics EXPRESS

Non-Markovian effect enhanced quantum noises in a coherent Ising machine

Chen-Rui Fan,[1] Bo Lu,[2,5] Yi-Xuan Yao,[3,4] Qing Ai,[3,4] and Chuan Wang[1,6]

[1] School of Artificial Intelligence, Beijing Normal University, Beijing, 100875, China
[2] Laboratory for Advanced Computing and Intelligence Engineering, Zhengzhou, 450001, China
[3] School of Physics and Astronomy, Applied Optics Beijing Area Major Laboratory, Beijing, 100875, China
[4] Key Laboratory of Multiscale Spin Physics, Ministry of Education, Beijing Normal University, Beijing 100875, China
[5] lubo@mail.bnu.edu.cn
[6] wangchuan@bnu.edu.cn

Abstract: Combinatorial optimization problems (COPs) constitute a fundamental class of computational challenges with extensive applications across scientific and industrial domains. The emergence of the coherent Ising machine (CIM) as a computational paradigm has demonstrated exceptional capabilities in rapidly generating arbitrary spin configurations and effectively solving large-scale COPs. Despite its promising potential, the CIM framework encounters an inherent limitation related to amplitude heterogeneity. Current approaches to this limitation primarily rely on Gaussian approximations to model quantum noise in the system's amplitude dynamics within the original CIM framework. However, these methods generally fail to account for the temporal and periodic non-Markovian characteristics of pulses in practical environments. In this study, we introduce temporally correlated non-Markovian noise into the dynamics of both conventional and spiking neural network-based CIM systems, investigating their performance through comprehensive hyperparameter analysis. Our method incorporates a detailed examination of hyperparameter selection and its influence on algorithmic efficiency. Through extensive numerical simulations, we demonstrate that the integration of non-Markovian noise significantly accelerates variance evolution in both canonical coordinates and amplitude dynamics over time. The proposed approach not only exhibits enhanced computational performance but also shows superior scalability for large-scale problem instances. These findings suggest that our approach offers distinct advantages in addressing complex COPs, potentially opening new avenues for efficient optimization in various applications.

1. Introduction

Combinatorial Optimization Problems (COPs) focus on identifying optimal combinations or configurations from a given set of possibilities and are prevalent in numerous domains, including logistics and transportation, network design, manufacturing, and financial investment [1,2]. These problems can be broadly characterized as the minimization or maximization of an objective function subject to specific constraints. However, COPs are typically classified as NP-hard, meaning that the computational time required to solve them grows exponentially with the size of the parameter space. This inherent complexity poses significant challenges for finding efficient solutions, particularly as the scales of the problems increase.

This inherent complexity presents substantial challenges in the resolution of large-scale instances of these problems. Over the years, researchers have developed a variety of heuristic algorithms, including simulated annealing, ant colony optimization, and particle swarm optimization [3–5]. These methods efficiently explore solution spaces by emulating natural processes. However, the lack of precise models often results in prohibitively long computation

#562816 https://doi.org/10.1364/OE.562816
Journal © 2025 Received 19 Mar 2025; revised 17 Apr 2025; accepted 27 Apr 2025; published 19 May 2025

Optics EXPRESS

times. Recently, physicists have introduced innovative computing paradigms to tackle COPs, such as Quantum Annealers, Ising Machines, Josephson parametric oscillators, and Semiconductor Annealers [6–10], which leverage phase transitions in the Ising model. These novel approaches have shown remarkable improvements in both computational efficiency and solution accuracy compared to traditional algorithms, offering promising avenues to address complex optimization challenges.

The Coherent Ising Machine (CIM), rooted in the Ising model, has emerged as a highly effective computational framework to solve COPs [9,11,12]. This system enables arbitrary spin coupling and can solve large-scale COPs efficiently in short timeframes. The principle of CIMs is based on dynamic bifurcation, where spin amplitudes are mapped to discrete binary outcomes, simulating computational bits through the relation $\sigma_i = sign(x_i)$ [13,14]. Typically, CIMs are implemented using degenerate optical parametric oscillators (DOPOs), with bifurcation achieved via phase-sensitive amplification (PSA). This process is intrinsically linked to quantum noise fluctuations [15,16]. However, conventional CIM models often assume that the noise follows a Gaussian distribution with Markovian properties, neglecting temporal correlations [17,18]. This assumption is problematic, as real physical environments frequently exhibit non-Markovian characteristics [19]. Currently, the predominant programmable CIMs use an optical ring feedback structure as their computing and storage core [20,21]. The measure-feedback system (MFB) implements arbitrary coupling Ising model behaviors by returning a portion of the signal output back to the input, offering more flexibility compared to fixed delay optical paths and on-chip optical Ising machines [21,22]. However, time-delayed optical pulses exhibit periodic temporal effects on feedback, which demonstrate non-Markovian characteristics. Recent studies on open quantum optical systems, including optical systems [23,24] and quantum simulations [25,26], have demonstrated that incorporating non-Markovian noise can lead to a variety of intriguing and practical applications. These findings highlight the potential of leveraging non-Markovian dynamics to enhance the performance and versatility of CIM-based systems.

Furthermore, the evolution of individual spins in CIMs can lead to divergent stable points due to the non-uniform coupling matrix, resulting in amplitude heterogeneity, a discrepancy between the ground state spin outcomes of the CIMs, and the ideal Ising model. To address this issue, several approaches have been proposed, including nonlinear filtering [27], error correction signals [28–30], discrete simulated bifurcation machines [31,32], and CIMs based on spiking neural networks (SNN-CIM) [33,34]. While these methods incorporate Gaussian approximations to model the quantum noise in the system's amplitude dynamics, they often treat the noise as purely Markovian. This simplification overlooks the inherent non-Markovian properties, such as time delay and periodicity, characteristic of real-world environments with optical pulses. Consequently, there remains a need to better account for these temporal correlations to further enhance the accuracy and efficiency of CIM-based solutions.

To address the limitation that random Gaussian noise fails to capture the time-correlated noise inherent in feedback systems, this paper introduces periodic non-Markovian noise into the evolution processes of both CIM and SNN-CIM. This approach aims to more accurately simulate the influence of environmental noise on computational models in open quantum systems, thereby better representing the evolution of Ising machines in real-world environments. By employing a Gaussian approximation to neglect higher-order fluctuation products and incorporating a tunable noise term influenced by multiple discrete moments, we derive the master equation for the evolution of the degenerate optical parametric oscillators (DOPOs). We further analyze the selection of key parameters in the model, as the choice of parameters depends on the type and scale of the problem graph and can significantly affect computational performance. Additionally, we compare the evolution of the DOPO process with and without the non-Markovian noise and evaluate the computational performance of the CIM and the SNN-CIM with noise across problems of varying scales. We believe that this work may further explore the relationship between Ising machine bifurcations and quantum noise and improve the computational performance of Ising machines in COP.

2. Dynamics of the system

2.1. Basic model

Currently, programmable CIMs with measure-feedback systems (MFB-CIMs) are widely employed to solve the COPs, as the optimal solution often corresponds to the spin configuration of the system in its ground state. For an N-spin system, each spin can take one of two states, $\sigma_i = \pm 1$, and the Ising Hamiltonian is defined by

$$H = -\frac{1}{2}\sum_{i,j} J_{ij}\sigma_i\sigma_j. \tag{1}$$

Here, J_{ij} represents the matrix coupling coefficient of the optical pulses. The value of J_{ij} can be any real number for different problems. In an MFB-CIM optical fiber ring, the amplitude results X_i are obtained through measurements of the output coupler, and the symbolic set of X_i represents the solution to the COP. The field programmable gate array (FPGA) computes the amplitude and phase of the injected term $I_{\text{inj}} = \sum J_{ij}X_j$. The photonic modulator then receives the injected pulse I_{inj} and couples it to the target pulse through the input coupler. After a period of evolution, the system is in the lowest energy state, and the corresponding problem is solved.

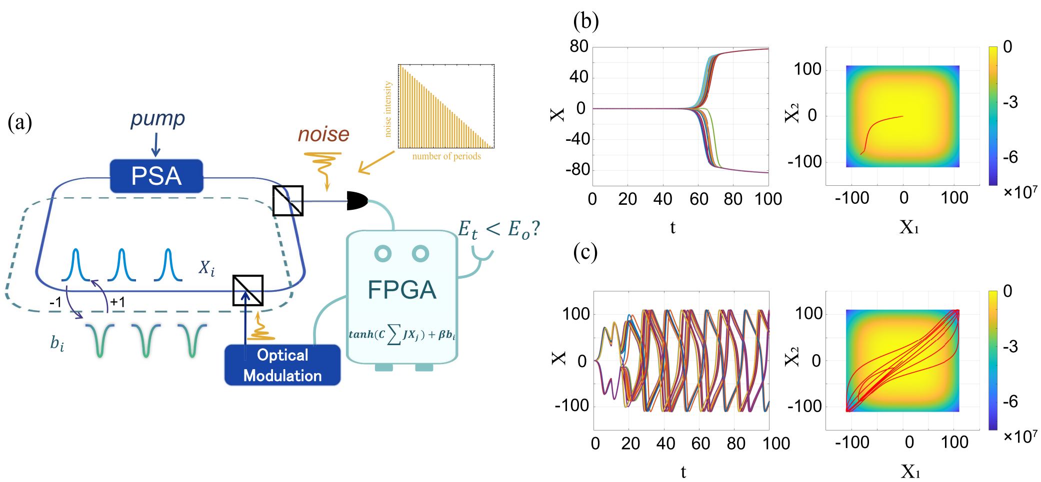

Fig. 1. (a)Schematic diagram of the SNN-CIM. The blue loop represents the X-type pulses, which are the DOPO pulses, while the green loop represents the error-correcting dissipative b-pulse. They are combined through an antisymmetric coupling. The yellow bar graph shows the noises in different delays. (b) and (c) show respectively the evolution of 25 spins over time for the CIM and SNN-CIM in solving the Max-Cut problem for a fully connected graph with 25 nodes, with the left showing all spins and the right focusing on the evolution of two spins towards the lowest energy state.

However, the amplitude heterogeneity in MFB-CIM can significantly degrade its computational performance. A fixed pump strength is unable to simultaneously optimize the states of all spins. When spin amplitudes are mapped to discrete binary outcomes using $\sigma_j = sign(x_j)$, errors can arise, leading to a mismatch between the ground state spin configuration of the MFB-CIM and that of the Ising model. This discrepancy can result in similar performance issues. The SNN-CIM, as illustrated in Fig. 1(a), provides an effective solution to the problem of amplitude heterogeneity. Similarly to the MFB-CIM, it employs a nonlinear function, $tanh(I_{\mathrm{inj}})$, to filter out non-uniform coupling terms, thereby alleviating the amplitude heterogeneity issue. Furthermore, the SNN-CIM introduces a dissipative b-pulse as an error correction signal, which destabilizes fixed points and enables the system to escape local minima during the computation process. This mechanism enhances the system's ability to converge toward more optimal solutions.

In Fig. 1(a), the blue loop represents the nonlinear optical fiber loop incorporating the PSA, where X-pulses correspond to the DOPO pulses. The green loop represents the dissipative b-pulse, which serves as an error correction mechanism. It is coupled in an oppositely symmetric manner with the X-pulse to form a spiking neuron. Coupling is achieved through input and output couplers with reflectivity R (where $R = j\Delta t$, R signifies the reflectivity of the out-coupling beam splitter, j is the injection coupling strength, and Δt denotes the temporal duration for a complete traversal of the ring cavity). Both the measurement and injection processes introduce vacuum quantum noise W and environmental noise ξ. By maintaining a fixed pump intensity and increasing the coupling term amplification factor C during computation, the ground-state energy can be minimized, allowing the system to search for solutions based on the principle of minimum gain.

The FPGA dynamically adjusts the antisymmetric coupling coefficient b based on the relationship between the real-time energy E_t and the lowest energy E_o before time t, thereby influencing the stability of the system's fixed points and enabling closed-loop control of the search process. The yellow bar graph illustrates that the non-Markovian environmental noise diminishes as the number of periods increases, indicating that earlier moments have a reduced influence on the current state. The intensity of the environmental noise injected into the system can be controlled by adjusting the parameter α. Figure 1(b) and (c) depict the computational processes of CIM and SNN-CIM, respectively, when solving the Max-Cut problem for a fully connected graph with 25 nodes. Notably, there is a significant difference in their search processes. In terms of the evolution of spin amplitudes and potential functions over time, SNN-CIM exhibits faster convergence and achieves the minimum potential energy multiple times, demonstrating its superior efficiency and robustness compared to traditional CIM.

Before introducing the quantum theoretical model of SNN-CIM, we begin with the master equation of the CIM [15]:

$$\frac{\partial \hat{\rho}}{\partial t} = \sum_r \left(\frac{\partial \hat{\rho}}{\partial t}\right)_{DOPO} + \left(\frac{\partial \hat{\rho}}{\partial t}\right)_{output} + \left(\frac{\partial \hat{\rho}}{\partial t}\right)_{input} \tag{2}$$

The three terms on the right side of the equation represent the evolution process of the DOPOs, the impact of the output, and the input coupler, respectively. The master equation of the r-th DOPO is defined by:

$$\left(\frac{\partial \hat{\rho}}{\partial t}\right)_r = ([\hat{a}_r, \hat{\rho}\hat{a}_r^\dagger] + \mathrm{H.c.}) + \frac{p}{2}[\hat{a}_r^{\dagger 2} - \hat{a}_r^2, \hat{\rho}] + \frac{g^2}{2}([\hat{a}_r^2, \hat{\rho}\hat{a}_r^{\dagger 2}] + \mathrm{H.c.}) \tag{3}$$

g is photon absorption coefficient and $\hat{a}_r$ is annihilation operator of the r-th signal mode. Terms on the right side sequentially represent the linear dissipation of signal photons and the nonlinear interaction between signal and pump photons. The DOPO pulse in-phase amplitude at each round trip is $\hat{X}_r = \frac{\hat{a}_r + \hat{a}_r^\dagger}{2}$ and $\Delta\hat{X}_r = \hat{X}_r - \langle \hat{X}_r \rangle$. These nonlinear interactions allow the CIM to produce binarized outcomes at suitable pump intensities, rendering it highly effective for solving specific classes of COPs.

Optics EXPRESS

Table 1 are the converting operators to an equivalent c-number form by using the Glauber-Sudarshan representation for ρ[35]: After the transformation, Eq. 3 could be expressed as:

$$\begin{aligned}\frac{\partial P}{\partial t} &= \frac{\partial}{\partial \alpha_r}(\alpha_r P) - p\frac{\partial}{\partial \alpha_r}(\alpha_r^\dagger P) + g^2\frac{\partial}{\partial \alpha_r}(\alpha_r^\dagger \alpha_r^2 P) + \frac{1}{2}\frac{\partial^2}{\partial \alpha_r^2}(p - g^2\alpha_r^2) \\ &+ \frac{\partial}{\partial \alpha_r^\dagger}(\alpha_r^\dagger P) - p\frac{\partial}{\partial \alpha_r^\dagger}(\alpha_r P) + g^2\frac{\partial}{\partial \alpha_r^\dagger}(\alpha_r^{\dagger 2}\alpha_r P) + \frac{1}{2}\frac{\partial^2}{\partial \alpha_r^{\dagger 2}}(p - g^2\alpha_r^{\dagger 2})\end{aligned} \tag{4}$$

So the equivalent positive-Pc-number stochastic differential equations (c-SDEs) is:

$$\frac{d\alpha_r}{dt} = -\alpha_r + p\alpha_r^\dagger - g^2\alpha_r^\dagger\alpha_r^2 + \sqrt{p - g^2\alpha_r^2}\,\xi_{1,r} \tag{5}$$

$$\frac{d\alpha_r^\dagger}{dt} = -\alpha_r^\dagger + p\alpha_r - g^2\alpha_r^{\dagger 2}\alpha_r + \sqrt{p - g^2\alpha_r^{\dagger 2}}\,\xi_{2,r} \tag{6}$$

Table 1. Glauber-Sudarshan representation

$a\rho$	$\leftrightarrow$	$\alpha P(\alpha)$
$a^\dagger\rho$	$\leftrightarrow$	$\left(\alpha^* - \frac{\partial}{\partial\alpha}\right)P(\alpha)$
ρa	$\leftrightarrow$	$\left(\alpha - \frac{\partial}{\partial\alpha^*}\right)P(\alpha)$
$\rho a^\dagger$	$\leftrightarrow$	$\alpha^* P(\alpha)$
$a^\dagger a\rho$	$\rightarrow$	$\left(\alpha^* - \frac{\partial}{\partial\alpha}\right)\alpha P$
$\rho a^\dagger a$	$\rightarrow$	$\left(\alpha - \frac{\partial}{\partial\alpha^*}\right)\alpha^* P$

Building on this foundation, the SNN-CIM incorporates spiking neurons, illustrated by the green pulses in Fig. 1(a). Each spiking neuron is formed through an antisymmetric coupling between an X-pulse and a b-pulse, where the neuron's state is determined by the amplitude of the X-pulse. The coupling matrix governing this interaction is given by $\begin{bmatrix} 0 & 1 \\ -1 & 0 \end{bmatrix}$. Following the measurement of the output coupler results by the FPGA, the pulses are modulated in amplitude using an optical modulator and subsequently injected back into the ring cavity. Here, $\xi_{a,r}$ represents random numbers satisfying specific statistical properties.

$$\begin{aligned}\langle \xi_{a,r}(t)\xi_{b,r'}(t')\rangle = \delta_{ab}\delta_{rr'}\Bigg\{&\delta(t-t') + \alpha\sum_{k=1}^{K} e^{-jk\Delta t}\Big[\sqrt{1 - j\Delta t}\,\delta(t - t' - k\Delta t)e^{ik\varphi} \\ &+ \sqrt{j\Delta t}\,\delta(t - t' + k\Delta t)e^{-ik\varphi}\Big]\Bigg\}\end{aligned} \tag{7}$$

The second and third terms in curly braces represents the effects caused by non-Markovian dynamics [36] which is related to α , K and j . They represent the intensity of the non-Markovian effect ,time range of its impact and injection coupling strength, respectively. Each output of the subsystem drives another subsystem, with propagation delays Δt occurring in both directions. Conversely, each subsystem is influenced by delays Δt and $-\Delta t$. The exponential term $(e^{-jk\Delta t})$ is introduced as a decay factor to account for the diminishing influence of earlier states on the current result as $k\Delta t$ increases. After applying the Gaussian approximation, the dynamic evolution process of the SNN-CIM can be described as follows:

$$\begin{aligned}\frac{d\mu_r}{dt} &= -(1-p+j)\mu_r - g^2(\mu_r^2 + 2n_r + m_r)\mu_r \\ &+ \sqrt{j}(m_r + n_r)W_r - j\gamma_b b \\ &+ tanh\{Cj\sum_{r'}\tilde{J}_{rr'}\left(\mu_{r'} + \sqrt{\frac{1}{4j}}W_{r'}\right)\}\end{aligned} \tag{8}$$

$$\frac{dn_r}{dt} = -2(1+j)n_r + 2pm_r - 2g^2\mu_r^2(2n_r + m_r) - Fj(m_r + n_r)^2 \tag{9}$$

$$\begin{aligned}\frac{dm_r}{dt} &= -2(1+j)m_r + 2pn_r - 2g^2\mu_r^2(2m_r + n_r) \\ &+ F\left[p - g^2(\mu_r^2 + m_r) - j(m_r + n_r)^2\right]\end{aligned} \tag{10}$$

$$\frac{db_r}{dt} = -\gamma_b b + j\left(\mu_r + \frac{W_r}{\sqrt{4j}}\right) \tag{11}$$

$$F = 1 + \alpha\sum_{k=1}^{K} e^{-jk\Delta t}\left(\sqrt{1 - j\Delta t}e^{i\varphi} + \sqrt{j\Delta t}e^{-i\varphi}\right) \tag{12}$$

Here, b represents the dissipative pulse amplitude, F represents the form after transformation of Eq. 7, and W denotes the vacuum noise caused by homodyne measurement and feedback injection. We can separate α_r into the mean field and small fluctuation as $\alpha_r = \langle\alpha_r\rangle + \Delta\alpha_r$ and $\alpha_r^\dagger = \langle\alpha_r^\dagger\rangle + \Delta\alpha_r^\dagger$ by using the Gaussian approximation. The mean value of the amplitude is $\mu_r = \langle\alpha_r\rangle = \langle\alpha_r^\dagger\rangle$, with fluctuations are $m_r = \langle\Delta\alpha_r^2\rangle = \langle\Delta\alpha_r^{\dagger 2}\rangle$ and $n_r = \langle\Delta\alpha_r\Delta\alpha_r^\dagger\rangle$. The variance in canonical coordinate is $\langle\Delta\hat{X}_r^2\rangle = m_r + n_r + \frac{1}{2}$ and the variance in canonical momentum could be described as $\langle\Delta\hat{P}_r^2\rangle = -m_r + n_r + \frac{1}{2}$.

Therefore, the dynamic equation of SNN-CIM incorporating non-Markovian noise can be derived. In subsequent numerical simulations, these differential equations will be solved using the Euler method. In the CIM framework, once the spin amplitudes evolve to minimize the system energy, the resulting spin configuration is fully determined. However, in SNN-CIM, the system is reset to an unstable state by adjusting the parameter γ_b of the b-type pulses, which is shown in Fig. 2. This structure allows it to search between low-energy states and effectively escape from the constraints of local minima. During the initial condition t<400, the system searches for the ground state in Fig. 2(a). The energy of the spin configuration, described by $E = -\frac{1}{2}J\sigma_i\sigma_j$, gradually decreases. This reduction occurs while the pump strength remains constant and the coupling term amplification factor C is increased, as depicted in Fig. 2(d), indicating that the system is in an effective search stage. The energy of the system suddenly increases because the algorithm decreases the antisymmetric coupling coefficient γ_b when the system evolves to a local minimum or an excited state, placing the parameters in the instability region of the fixed point and allowing the system to continue its search effectively [34]. When t>400, the energy value obtained during the effective search phase reaches its minimum. Here we set the threshold time to 100 iterations. The algorithm then resets the coupling term amplification factor C to its initial value every 100 iterations, initiating a new cycle of search. This iterative process ensures that the system continues to explore and converge toward optimal solutions.

2.2. Optimal parameters for the system

In the SNN-CIM model, parameters j and p represent the output coupling rate and the linear gain coefficient, both of which significantly influence computational performance. To determine

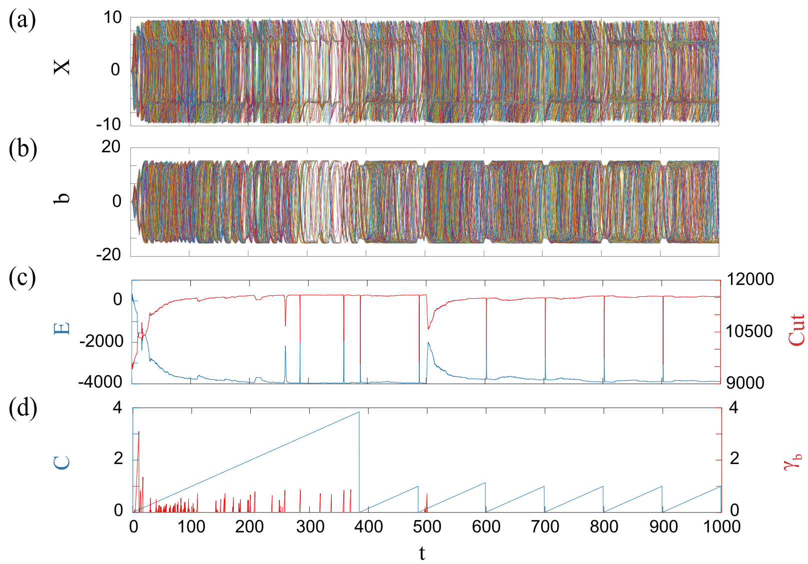

Fig. 2. The evolution of X-pulses and b-pulses over computation time is shown in (a) and (b). (c) and (d) illustrate how adjusting the dissipation and coupling term amplification factor in the SNN-CIM model affects the stability of its nonlinear dynamical system, thereby preventing the system from being trapped in local minima.

the optimal parameters, we show the effect of different combinations of parameters on the computational performance of the model in Fig. 3. Time-to-solution (TTS) is selected to evaluate the performance, which is calculated using $T \log(1-0.99)/\log(1-P_S)(TTS = T$ when $P_S = 1)$. Here, T is the time taken for each trial computation, P_S is the probability of obtaining the Max-Cut value, and TTS represents the computation time required to find the optimal value with a 99% probability. Our objective is to determine the values of j and p that minimize TTS, thereby optimizing the model's computational efficiency.

For CIM with $d = 0.3$, the parameters that achieve smaller TTSs are generally distributed around the linear range $p = j + 1$ in Fig. 3(a). When $p<1$, the total gain of the system is lower than the inherent dissipation, preventing stable bifurcation and making it impossible to obtain the ground state spin configuration. For the fully connected graphs that exhibit high symmetry and numerous degenerate ground states (as shown in the second row), achieving stable bifurcation requires only $p>j+1$. Similarly, in the SNN-CIM framework, the graph with $d = 0.3$ has stricter requirements for the values of j and p compared to the fully connected graph. For sparse graphs, the value of p needs to satisfy $1+j<p<2.5+j$, whereas for $d = 1.0$, $p>1+j$ is sufficient to achieve good computational results. Therefore, in the numerical simulations that follow, we choose $p = 2 + j$ to ensure the computation is more efficient.

The photon absorption coefficient g also plays a critical role in determining the computation success rate of both CIM and SNN-CIM. This parameter quantifies the loss of two photons as the pulse passes through the PSA in the DOPO. As g^2 increases, the number of excited pump photons decreases, causing a shift in the nonlinear fixed points within the evolution equations. This shift ultimately impacts the computational accuracy of the models. The amplitude evolution equation for a noiseless single DOPO is given by $\dot{\mu} = (p-j-1)\,\mu - g^2\mu^3$, derived from Eq. 8. Figure 4 demonstrates that as g^2 increases, the degree of bifurcation initially rises and then declines, reaching a peak within the range $10^{-2}<g^2<10^{-1}$. Therefore, for subsequent numerical

Optics EXPRESS

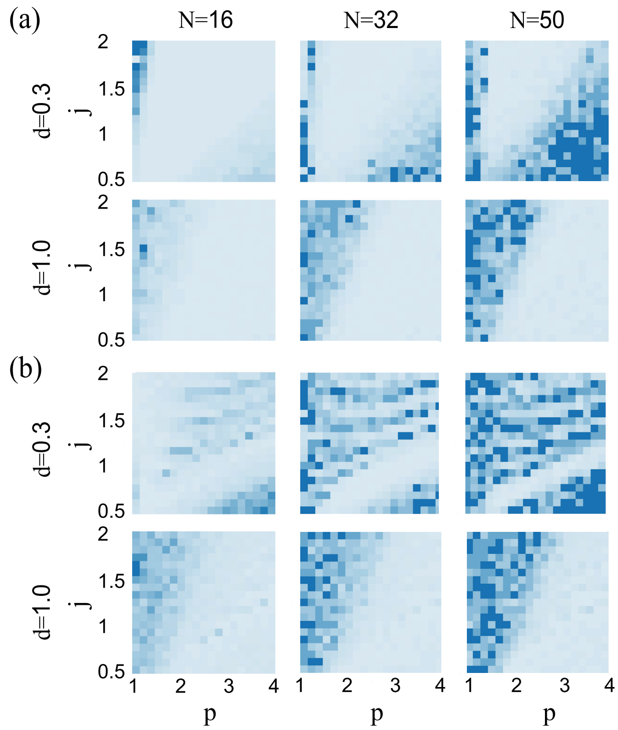

Fig. 3. The impact of j and p on the computational performance of CIM (a) and SNN-CIM(b) varies with different graph scales and sparsity conditions. For both models, the first and second rows display computational results for sparse and fully connected graphs, respectively. The first, second, and third columns represent graphs with scales of 16, 32, and 50, respectively, in increasing order. The color of the block in each small picture represents the TTS value of the system at the value of j and p on the horizontal and vertical coordinates at this time. The darker the color, the larger the TTS value. $\alpha = 0.05$ was used to illustrate the impact of non-Markovian noise on system performance and ensure accurate model computations.

simulations, g^2 values will be selected from this optimal range to ensure the best computational performance.

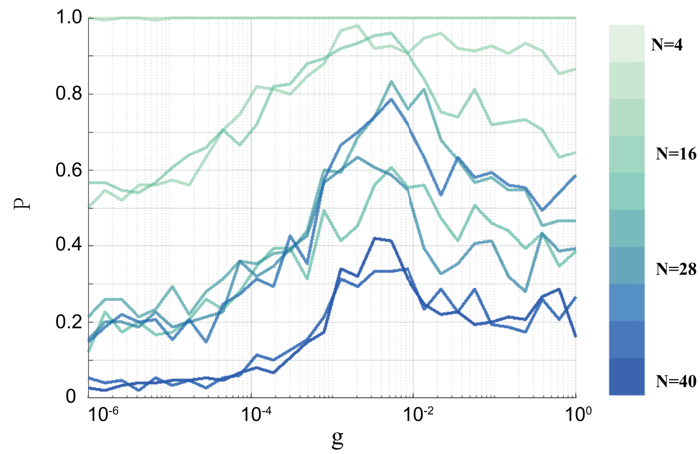

Fig. 4. The success rate of SNN-CIM on sparse graphs of varying scales with $d = 0.5$ and different values of g^2. The intensity of the line color indicates the value of N, with darker colors corresponding to larger N values. The difference in N values represented by adjacent colors is 4.

3. Results

When the CIM simulates the evolution of the Ising model, differences in pump thresholds and coupling matrices can prevent bifurcation phenomena, often leading to amplitude exponential explosion–an abnormal state during the simulation. To ensure the model's correct operation, we first investigated its dynamic processes. In Fig. 5, we observe that the introduction of non-Markovian noise accelerates the evolution of variance in both canonical coordinates and amplitudes for both CIM and SNN-CIM.Furthermore, even with this noise, SNN-CIM maintains a faster computation speed compared to CIM, highlighting the enhanced computational performance resulting from the incorporation of b-pulses. This improvement arises because non-Markovian noise amplifies second-order correlated noise by influencing pulses at different times. Since the optimal solution for the anti-ferromagnetic coupling matrix is $\sigma_1 = 1$ and $\sigma_2 = -1$, the amplitude evolution results for all four models in Fig. 5(b) consistently exhibit one amplitude increasing while the other decreases.

The antiferromagnetic coupling matrix is overly simplistic as a problem matrix. In Fig. 6, we evaluate a more complex problem to compare the computational speed differences between CIM and SNN-CIM. For both models, the computation time significantly influences the success rate of the computation, where success is defined by achieving the Max-Cut value. When the computation time is insufficient, the majority of cases remain unresolved. As the computation time increases, the number of unresolved cases decreases until the computation time is sufficiently long to ensure all cases achieve an optimal value. Here, we primarily focus on the model's computation speed. A faster decline in the curve indicates that SNN-CIM reaches the optimal solution more frequently with the same number of iterations or that SNN-CIM achieves similar results to CIM in a shorter amount of time. This advantage arises from introducing the dissipative b-pulse in SNN-CIM, which makes the system more likely to enter unstable states. This allows the system to more rapidly explore different spin configurations, avoiding the problem of getting stuck in local optima that is common in CIM, and also speeds up computation. The observed phenomenon is further corroborated by Fig. 1(b) and (c). Besides, the models incorporating non-Markovian noise show faster computational speed, as the addition of noise accelerated the bifurcation of spin amplitude.

Optics EXPRESS

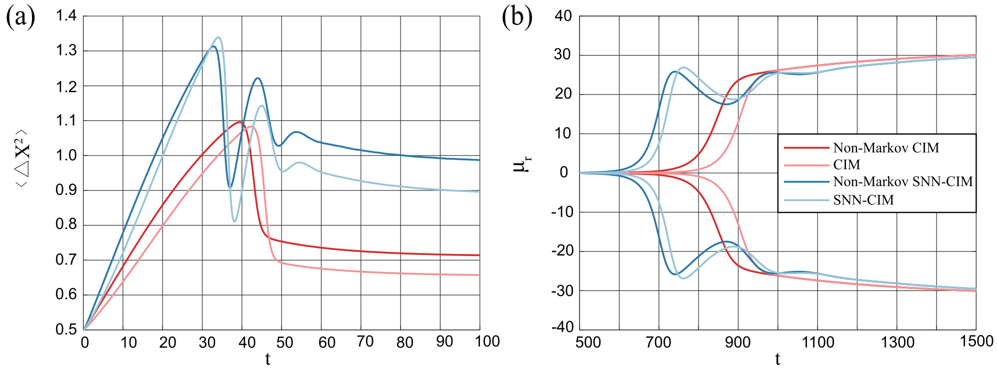

Fig. 5. The evolution of variance in canonical coordinate and amplitude over time for CIM and SNN-CIM after introducing non-Markovian noise. The four models here all compute the simplest antiferromagnetic coupling matrix.

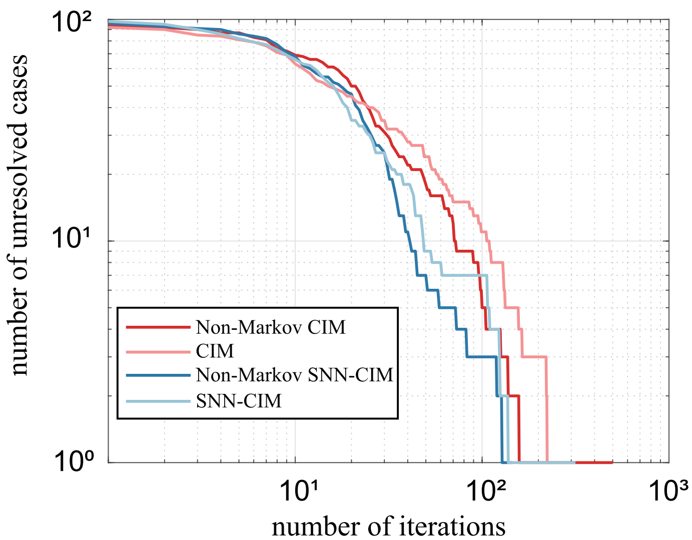

Fig. 6. The relationship between unresolved compute cases and compute time. 1000 compute cases were computed on a coupled matrix element of 0 or 1 with sparsity $d = 1.0$ and $N = 500$.

Next, in Fig. 7, we compare the TTS and the fitted curves of CIM and SNN-CIM with non-Markovian noise for different graph scales, with the results being fit to an exponential model of the form $p \cdot q^{\sqrt{x}}$. Table 2 presents the numerical results of the fits. It can be concluded that for both types of problem graphs, the base value q for SNN-CIM is significantly lower than that for CIM. This indicates that as the problem graph size $\sqrt{N}$ increases, the TTS growth rate for SNN-CIM is slower, implying that SNN-CIM computes faster and is more suitable for large-scale problems. However, the pump p for SNN-CIM is relatively large. The result is that SNN has more parameters and more complex search mechanism, which makes it less beneficial for tackling simpler problems. It can be seen that the CIM only computes to $N = 35$, because the optimal value computed by SNN-CIM is used as the test criterion to define whether the computation is successful, and the CIM cannot compute the optimal value at a scale greater than 35, and the success rate is 0, which makes the TTS value meaningless. The data points with small N

Optics EXPRESS

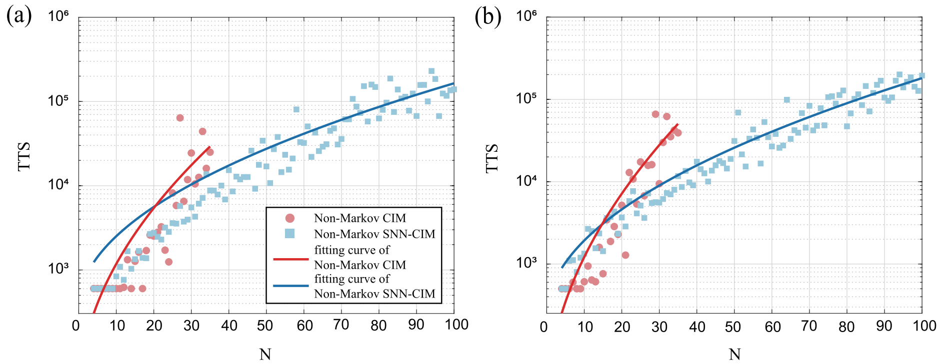

Fig. 7. The variation in TTS for CIM and SNN-CIM across different graph sizes is analyzed, with the results being fit to an exponential model of the form $p \cdot q^{\sqrt{x}}$. The blue and pink points represent the simulation results of TTS of CIM and SNN-CIM under different N. The blue and pink curves represent the fitting results of CIM and SNN-CIM. (a)The coupling matrix elements are either 0 or 1 with $d = 0.5$. (b)The elements are 21 equally spaced decimal values between -1 and 1.

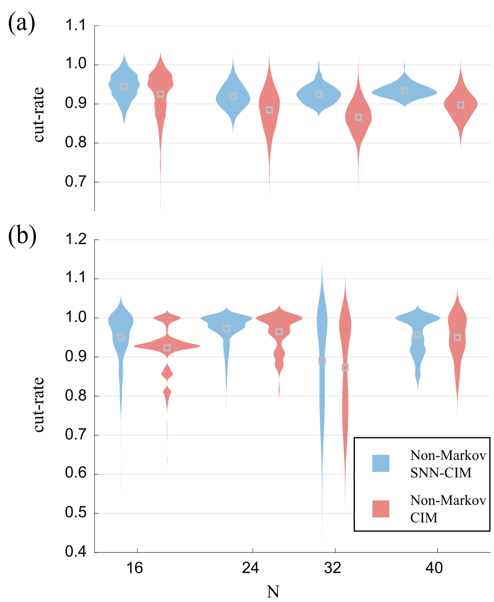

Fig. 8. The statistical distribution of cut-rate from 500 computations for graphs of different sizes is analyzed. For adjacent, similarly colored violin plots, the lighter color on the left represents SNN-CIM statistics, while the right represents CIM. The gray grid indicates the mean value of the cut-rate. (a) represents a series of graphs where the elements of the coupling matrix used in the computations are either 0 or 1, with a sparsity of $d = 0.5$. (b) represents a series of graphs where the elements of the coupling matrix used in the computations are decimal values uniformly distributed between $[-1, 1]$, with 21 discrete values.

values have obvious deviations from the fitting curves because the problem size is too small, the computation time is relatively sufficient, and the computation accuracy is high, resulting in a small TTS value. As N increases, the complexity of the problem increases rapidly, the computation success rate decreases, and the TTS value increases rapidly.

Table 2. TTS fitting results for CIM and SNN-CIM

	$\{0, 1\}$ $d = 0.5$		[-1,1]	
	CIM	SNN-CIM	CIM	SNN-CIM
p	29.56	363.60	16.80	236.30
q	3.21	1.84	3.87	1.94

More importantly, in addition to its advantage in computing speed, SNN-CIM also outperforms CIM in accuracy. Figure 8 shows a statistical analysis of 500 computational results for the cut-rate (defined as the ratio of the cut to the Max-Cut) across various graph sizes, comparing SNN-CIM (left) with CIM (right). We use cut-rate here because cut values increase with problem size, which causes the shape of individual violin plots to shrink, making the distribution of solutions less discernible. The range of cut-rate is between [0, 1]. Logically, each violin plot should also be within this range. The wider the shape, the more distribution there is in this cut-rate value. However, since the kernel density estimation of the violin function will smooth the data and extend to a certain extent outside the data range, the violin plot in Fig. 8 has a value greater than 1, but this does not affect our observation of the distribution of the computation results. In these plots, the area of each rectangular colored block represents the number of occurrences of the cut-rate within that vertical coordinate range. Firstly, for each problem size N, the mean cut rate of SNN-CIM is higher than that of CIM. Secondly, in terms of the distribution of the violin plot, the color blocks with higher cut-rate values of SNN-CIM are larger, while the color blocks with lower cut-rate values are smaller. This shows that the computation results of SNN-CIM for different scales are higher than those of CIM. Compared with CIM, the solutions of SNN-CIM are often distributed in the part closer to the optimal value. This advantage is because the b-pulse added to SNN-CIM can correct the amplitude heterogeneity problem existing in CIM and avoid the nonlinear function causing the system to fall into the local minimum. The specific search process is described in detail in the model section.

4. Conclusion

To simulate the dynamic of the CIM operating in a real environment, we introduced adjustable non-Markovian environmental noise based on the CIM and SNN-CIM and analyzed its impact on parameter selection and computational performance. For the parameters such as j, p, and g, we obtained the computation results in all cases by traversing and selecting the parameter values used in subsequent numerical simulations by TTS. This parameter selection method can also be extended to other algorithms based on CIM, even if such behavior will cause a certain consumption of classical computing resources. Because of these parameters significantly influence whether CIM can be in a normal computational state according to Eq. 8 and blind attempts will cause more resource waste. We found that in Fig. 3, for the same graph density of the same problem, the law of its j and p value is stable, which can improve the efficiency of parameter estimation to a certain extent.

In numerical simulations, the inclusion of non-Markovian noise accelerated the evolution of variance in both canonical coordinates and amplitudes for both CIM and SNN-CIM. However, SNN-CIM consistently demonstrated faster computation speeds, particularly for large-scale graphs. In contrast, the CIM exhibited limitations, such as failing to achieve optimal solutions within the same computation time and displaying a large exponential base in the fitted TTS curve. Though the TTS of CIM is lower than that of SNN-CIM for small-scale problems due to the structure of SNN-CIM is more complex. But this does not affect the computational advantage of it as we usually expect to solve large-scale problems in fact. Finally, after statistical analysis of the cut-rate, the computation results of SNN-CIM are higher in terms of both the mean and the distribution of the results.

CIMs based on optical parametric oscillation have already demonstrated remarkable capabilities, such as solving Max-Cut problems with 100,000 spins at high speeds [22] while offering advantages in energy efficiency, speed, and solution quality [37]. The development of CIMs has pioneered new avenues for addressing COPs and has found applications in diverse fields, including wireless communications, chemical synthesis, and financial analysis. Moreover, the integration of CIMs with artificial intelligence holds significant promise, potentially accelerating deep neural network training [38–41] and driving future advances in artificial intelligence. This synergy between CIMs and AI is expected to play a pivotal role in the continued growth and innovation of intelligent systems.

Funding. National Natural Science Foundation of China (62461160263, 62401628, 62371050).

ACKNOWLEDGMENT. The authors gratefully acknowledge the support from the National Natural Science Foundation of China through Grants Nos. 62461160263, 62401628, and 62371050.

Disclosures. The authors declare no conflicts of interest.

Data availability. Data underlying the results presented in this paper are not publicly available at this time but may be obtained from the authors upon reasonable request.

References

1. C. Blum and A. Roli, "Metaheuristics in combinatorial optimization: Overview and conceptual comparison," ACM Comput. Surv. **35**(3), 268–308 (2003).
2. Y. Bengio, A. Lodi, and A. Prouvost, "Machine learning for combinatorial optimization: a methodological tour d'horizon," European Journal of Operational Research **290**(2), 405–421 (2021).
3. S. Kirkpatrick, C. D. Gelatt Jr, and M. P. Vecchi, "Optimization by simulated annealing," Science **220**(4598), 671–680 (1983).
4. M. Dorigo, V. Maniezzo, and A. Colorni, "Ant system: optimization by a colony of cooperating agents," IEEE Trans. Syst., Man, Cybern. B **26**(1), 29–41 (1996).
5. Y. Zhang, S. Wang, and G. Ji, "A comprehensive survey on particle swarm optimization algorithm and its applications," Math. Probl. Eng. **2015**, 1–38 (2015).
6. S. Boixo, V. N. Smelyanskiy, A. Shabani, *et al.*, "Computational multiqubit tunnelling in programmable quantum annealers," Nat. Commun. **7**(1), 10327 (2016).
7. A. K. Singh, K. Jamieson, P. L. McMahon, *et al.*, "Ising machines' dynamics and regularization for near-optimal mimo detection," IEEE Trans. Wireless Commun. **21**(12), 11080–11094 (2022).
8. S. Razmkhah, M. Kamal, N. Yoshikawa, *et al.*, "Josephson parametric oscillator based ising machine," Phys. Rev. B **109**(1), 014511 (2024).
9. N. Mohseni, P. L. McMahon, and T. Byrnes, "Ising machines as hardware solvers of combinatorial optimization problems," Nat. Rev. Phys. **4**(6), 363–379 (2022).
10. M. Yamaoka, C. Yoshimura, M. Hayashi, *et al.*, "A 20k-spin ising chip to solve combinatorial optimization problems with cmos annealing," IEEE J. Solid-State Circuits **51**, 1–3 (2015).
11. Y. Yamamoto, K. Aihara, T. Leleu, *et al.*, "Coherent ising machines-optical neural networks operating at the quantum limit," npj Quantum Information **3**(1), 49 (2017).
12. B. Lu, L. Liu, J.-Y. Song, *et al.*, "Recent progress on coherent computation based on quantum squeezing," AAPPS Bull. **33**(1), 7 (2023).
13. A. Marandi, Z. Wang, K. Takata, *et al.*, "Network of time-multiplexed optical parametric oscillators as a coherent ising machine," Nat. Photonics **8**(12), 937–942 (2014).
14. Z. Wang, A. Marandi, K. Wen, *et al.*, "Coherent ising machine based on degenerate optical parametric oscillators," Phys. Rev. A **88**(6), 063853 (2013).
15. Y. Inui, M. D. S. H. Gunathilaka, S. Kako, *et al.*, "Control of amplitude homogeneity in coherent ising machines with artificial zeeman terms," Commun. Phys. **5**(1), 154 (2022).
16. D. Maruo, S. Utsunomiya, and Y. Yamamoto, "Truncated wigner theory of coherent ising machines based on degenerate optical parametric oscillator network," Phys. Scr. **91**(8), 083010 (2016).
17. L. Luo, H. Liu, N. Huang, *et al.*, "Speed-up coherent ising machine with a squeezed feedback system," Opt. Express **28**(2), 1914–1926 (2020).
18. Y. Inui, E. Ng, and Y. Yamamoto, "Skew-gaussian model of small-photon-number coherent ising machines," arXiv (2024).
19. I. De Vega and D. Alonso, "Dynamics of non-markovian open quantum systems," Rev. Mod. Phys. **89**(1), 015001 (2017).

Optics EXPRESS

20. T. Inagaki, Y. Haribara, K. Igarashi, *et al.*, "A coherent ising machine for 2000-node optimization problems," Science **354**(6312), 603–606 (2016).
21. P. L. McMahon, A. Marandi, Y. Haribara, *et al.*, "A fully programmable 100-spin coherent ising machine with all-to-all connections," Science **354**(6312), 614–617 (2016).
22. T. Honjo, T. Sonobe, K. Inaba, *et al.*, "100,000-spin coherent ising machine," Sci. Adv. **7**(40), eabh0952 (2021).
23. N. Német and S. Parkins, "Enhanced optical squeezing from a degenerate parametric amplifier via time-delayed coherent feedback," Phys. Rev. A **94**(2), 023809 (2016).
24. B.-H. Liu, L. Li, Y.-F. Huang, *et al.*, "Experimental control of the transition from markovian to non-markovian dynamics of open quantum systems," Nat. Phys. **7**(12), 931–934 (2011).
25. X. Long, W.-T. He, N.-N. Zhang, *et al.*, "Entanglement-enhanced quantum metrology in colored noise by quantum zeno effect," Phys. Rev. Lett. **129**(7), 070502 (2022).
26. X. Yang, X. Long, R. Liu, *et al.*, "Control-enhanced non-markovian quantum metrology," Commun. Phys. **7**(1), 282 (2024).
27. F. Böhm, T. V. Vaerenbergh, G. Verschaffelt, *et al.*, "Order-of-magnitude differences in computational performance of analog ising machines induced by the choice of nonlinearity," Commun. Phys. **4**(1), 149 (2021).
28. T. Leleu, Y. Yamamoto, P. L. McMahon, *et al.*, "Destabilization of local minima in analog spin systems by correction of amplitude heterogeneity," Phys. Rev. Lett. **122**(4), 040607 (2019).
29. S. Kako, T. Leleu, Y. Inui, *et al.*, "Coherent ising machines with error correction feedback," Adv. Quantum Technol. **3**(11), 2000045 (2020).
30. S. Reifenstein, S. Kako, F. Khoyratee, *et al.*, "Coherent ising machines with optical error correction circuits," Adv. Quantum Technol. **4**(11), 2100077 (2021).
31. H. Goto, K. Tatsumura, and A. R. Dixon, "Combinatorial optimization by simulating adiabatic bifurcations in nonlinear hamiltonian systems," Sci. Adv. **5**(4), eaav2372 (2019).
32. H. Goto, K. Endo, M. Suzuki, *et al.*, "High-performance combinatorial optimization based on classical mechanics," Sci. Adv. **7**(6), eabe7953 (2021).
33. B. Lu, C.-R. Fan, L. Liu, *et al.*, "Speed-up coherent ising machine with a spiking neural network," Opt. Express **31**(3), 3676–3684 (2023).
34. B. Lu, Y.-P. Gao, K. Wen, *et al.*, "Combinatorial optimization solving by coherent ising machines based on spiking neural networks," Quantum **7**, 11511151 (2023).
35. D. F. Walls and G. Milburn, *Quantum optics* (Springer, 1994).
36. S. Whalen, A. Grimsmo, and H. Carmichael, "Open quantum systems with delayed coherent feedback," Quantum Sci. Technol. **2**(4), 044008 (2017).
37. R. Hamerly, T. Inagaki, P. L. McMahon, *et al.*, "Experimental investigation of performance differences between coherent ising machines and a quantum annealer," Sci. Adv. **5**(5), eaau0823 (2019).
38. F. Böhm, D. Alonso-Urquijo, G. Verschaffelt, *et al.*, "Noise-injected analog ising machines enable ultrafast statistical sampling and machine learning," Nat. Commun. **13**(1), 5847 (2022).
39. J. Laydevant, D. Marković, and J. Grollier, "Training an ising machine with equilibrium propagation," Nat. Commun. **15**(1), 3671 (2024).
40. S. Niazi, N. Chowdhury, A. Aadit, *et al.*, "Training deep boltzmann networks with sparse ising machines," Nat. Electron. **7**(7), 610–619 (2024).
41. X. Song, T. Liu, S. E. Li, *et al.*, "Training multi-layer neural networks on ising machine," arXiv (2023).